ADVANCED MATERIALS
www.advmat.de

High-Performing and Capacitive-Matched Triboelectric Implants Driven by Ultrasound

Young-Jun Kim, Jiho Lee, Joon-Ha Hwang, Youngwook Chung, Byung-Joon Park, Junho Kim, So-Hee Kim, Junseung Mun, Hong-Joon Yoon, Sung-Min Park, and Sang-Woo Kim**

In implantable bioelectronics, which aim for semipermanent use of devices, biosafe energy sources and packaging materials to protect devices are essential elements. However, research so far has been conducted in a direction where they cannot coexist. Here, the development of capacitance-matched triboelectric implants driven is reported by ultrasound under 500 mW cm^{-2} safe intensity and realize a battery-free, miniatured, and wireless neurostimulator with full titanium (Ti) packaging. The triboelectric implant with high dielectric composite, which has ultralow output impedance, can efficiently deliver sufficient power to generate the stimulation pulse without an energy-storing battery, despite ultrasound attenuation due to the Ti, and has the highest energy transmission efficiency among those reported so far. In vivo study using a rat model demonstrated that the proposed device system is an effective solution for relieving urinary symptoms. These achievements provide a significant step toward permanently implantable devices for controlling human organs and treating various diseases.

1. Introduction

Active implantable medical devices (AIMDs), particularly neurostimulators, have been used to normalize physiological dysfunctions by delivering artificially generated stimulus to nerves governing the target functions. Clinically available applications of these devices include deep brain stimulation[1,2] for treating brain disorders, such as epilepsy and Parkinson's disease, spinal cord stimulation[3] for treating chronic pain, and peripheral nerve stimulation[4] for treating bladder disorders. While advancement of this technology has paved the way for nonpharmaceutical device solutions to manage intractable neurological diseases, the major drawback of this technology is the complications due to surgical procedures for the replacement of the device that has reached the end of its battery lifetime. In this context, AIMD requires a sustainable energy source for their semipermanent lifetime to avoid frequent surgeries, thus reducing patients' burden associated with the implantation procedure.[5]

Various energy harvesting technologies utilizing mechanical, solar, and thermal energy have been introduced to address the limited lifespan problem of AIMDs. Nonetheless, harvesting

Y.-J. Kim, J.-H. Hwang, Y. Chung
School of Advanced Materials Science and Engineering
Sungkyunkwan University (SKKU)
Suwon 16419, Republic of Korea

J. Lee, J. Mun, S.-M. Park
Department of Convergence IT Engineering
Pohang University of Science and Technology (POSTECH)
Pohang 37673, Republic of Korea
E-mail: ezo15@postech.ac.kr; sungminpark@postech.ac.kr

J.-H. Hwang, Y. Chung
Research and Development Center
Energymining Co., Ltd.
Suwon 16226, Republic of Korea

B.-J. Park, S.-H. Kim, S.-W. Kim
Department of Materials Science and Engineering
Yonsei University
Seoul 03722, Republic of Korea
E-mail: kimsw1@yonsei.ac.kr

J. Kim, S.-M. Park
School of Interdisciplinary Bioscience and Bioengineering
Pohang University of Science and Technology (POSTECH)
Pohang 37673, Republic of Korea

H.-J. Yoon
Department of Electronic Engineering
Gachon University
Seongnam 13120, Republic of Korea

S.-M. Park
Department of Electrical Engineering
Department of Mechanical Engineering
Pohang University of Science and Technology (POSTECH)
Pohang 37673, Republic of Korea

S.-W. Kim
Center for Human-Oriented Triboelectric Energy Harvesting
Yonsei University
Seoul 03722, Republic of Korea

The ORCID identification number(s) for the author(s) of this article can be found under https://doi.org/10.1002/adma.202307194

DOI: 10.1002/adma.202307194

sufficient energy within the body's constrained environment is challenging. Mechanical energy harvesting through organ movement produces low energy due to small input energy values.[6] In addition, the use of light and heat energy faces limitations due to the lack of light sources[7] and the constant body temperature.[8] Consequently, wireless power transfer (WPT) technology is considered the most suitable option for powering AIMDs.[9–12] However, the conventional WPT technologies based on electromagnetic (EM) field have fundamental challenges for AIMD applications. The WPT technologies based on the EM field are susceptible to the angle and distance between the power source and the receiver, and their power sources are strongly regulated because their temperature rise can damage living tissue (Note S1, Supporting Information). Furthermore, as the goal is to provide a semipermanent lifespan to AIMDs, which previously had a replacement cycle of approximately a decade even with primary batteries, titanium (Ti) becomes an essential packaging material for AIMDs (Note S1, Supporting Information). Unfortunately, EM field-based WPT technology is incompatible with the Ti packaging material necessary for long-term AIMD packaging (Figure S1, Supporting Information).

Ultrasound is a promising WPT energy source for AIMD, due to its safety verified in various medical fields (sensing,[13] monitoring,[14] therapy,[15] and even acoustic power transfer[16]) and its high penetration ability, even in metallic materials.[17] Recently, triboelectric nanogenerators (TENGs) based on the coupling effect of contact electrification and electrostatic induction have attracted particular attention as a useful harvesting technology of ultrasound energy.[17–19] TENGs can be applied in a wide range of medical fields, with advantages of diversity in material selection, and minimized system scale.[18,19] However, TENG-based WPT technologies for AIMD have yet to accomplish advances toward real-world applications due to the absence of a device platform for the system integration of TENG into AIMD. A critical obstacle to combining TENG and AIMD systems is the TENG's high internal electrical impedance.[20] Most electronic circuits of battery-free AIMDs should have a low impedance to minimize energy consumption, and avoid unnecessary energy waste. The impedance mismatch between TENG and AIMD substantially decreases the energy transmission efficiency by loading a very small voltage on the AIMD. Although several previous studies have reported an increase in WPT efficiency by improving energy harvesting circuits with additional switching circuits[21] and inductor coils,[22] their complex circuit design and large scale might hinder the application of TENGs in AIMDs known to require a miniaturized and simplified system. Thus, there is a considerable unmet need to reduce the internal impedance of TENGs.

Herein, we report a novel design of the ultrasound-driven TENG compatible with Ti packaging for battery-free, miniatured, and wireless-powered AIMDs, and find that a Ti-packaged TENG-powered implantable neurostimulator is useful for treating chronic diseases by controlling physiological functions. The high impedance of the current TENGs comes from their extremely low capacitance, due to their low permittivity dielectric materials. Thus, we newly developed a capacitance-matched and implantable TENG (CMI–TENG) using a composite material-based triboelectric layer consisting of a high dielectric copolymer matrix, poly(vinylidenefluoride-*co*-trifluoroethylene) (P(VDF–TrFE)), together with a high dielectric ceramic material, $CaCu_3Ti_4O_{12}$ (CCTO) particles. The composite of high dielectric matrix and particles improved the device's power output by enhancing charge trapping capability and decreasing the output impedance, enabling real-time operation of nerve stimulation circuit, despite a reduced output due to the ultrasound attenuation from the Ti encapsulation layer. The use of Ti as a packaging material provided both biocompatibility and stability to pass the FDA's evaluation criteria for the mechanical stability of implantable medical devices. Finally, to demonstrate the preclinical effectiveness, we utilized the CMI–TENG-based neurostimulator for tibial nerve stimulation to treat urinary symptoms. The results of increased bladder capacity and urination cycle indicated that the fabricated tibial nerve stimulator could effectively manage urinary dysfunctions, such as overactive bladder. Our development of efficiently power consuming and Ti-compatible implant technology based on the proposed CMI–TENG provides a prominent advance toward the battery-free and fully wireless AIMD by solving the old dilemma of typical commercial AIMDs; barely compatible between WPT and Ti-packaging. Thus, it significantly provides the potential feasibility of permanently implantable medical devices.

2. Results

2.1. Design of a Battery-Free Wireless Neurostimulation System

The aim of this work was to provide a proof-of-concept to confirm the feasibility of a battery-free and wireless neurostimulation system (**Figure 1**a). With impedance-optimized neurostimulation system, CMI–TENG can harvest 20 kHz of AC electrical energy, and produce a 2 Hz pulse wave through a battery-free circuit. The pulse wave can stimulate the tibial nerve, and treat the overactive bladder (Figure 1b). Figure 1c shows a real photographic image of the nerve stimulation system, while Figure 1d illustrates the overall structure of the neurostimulator. Figure S2, Supporting Information, shows the CMI–TENG fabrication process. We prepared a thin (≈10 μm thick) membrane (14 × 14 mm^2) of P(VDF–TrFE):CCTO composite film to have a vibrating membrane and a triboelectric layer (Figure S3, Supporting Information). The membrane was suspended on a thin 12 × 12 mm^2 copper (Cu) electrode made on a flexible printed circuit board (PCB), and covered with gold (Au). The membrane and PCB were covered by an adhesive layer, and connected to the circuit. The CMI–TENG was less than 1 mm in thickness. Finally, we packaged our CMI–TENG-based AIMD with Ti. A supporting jig was placed under the device to prevent shorting (Figure S4, Supporting Information). Figure 1e,g shows photographic images of an energy harvesting TENG and a pulse generation circuit.

The CMI–TENG operates in a single-electrode mode using the Au/Ni electrode as the primary electrode, and the P(VDF–TrFE):CCTO membrane as the triboelectric layer. When vibrating, the P(VDF–TrFE):CCTO membrane makes contact with the electrode, and the triboelectric phenomenon generates negative charge on the inner surface of the membrane. These charges can decrease the electrical potential of the electrode, compared to the reference, attracting holes in the electrode, and generating a current pulse in the circuit.[18,19] When separating, the electrode's potential increases, releasing holes in the circuit,

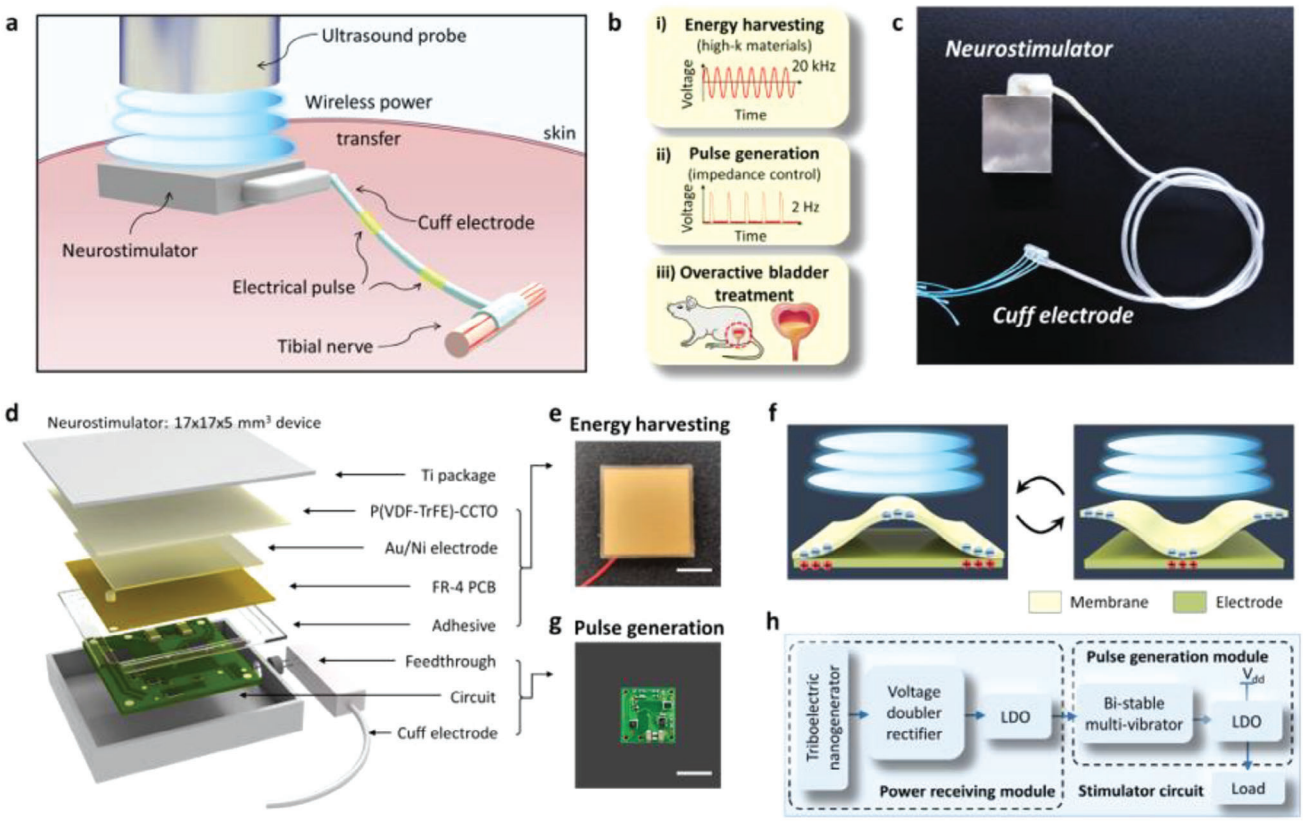

Figure 1. Battery-free, wireless, and Ti-packaged electroceuticals design. a) Schematics of the battery-free, wireless, and Ti-packaged nerve stimulation system. This consists of a nerve stimulator powered by ultrasound, and a cuff electrode for direct stimulation of the tibial nerve. b) The overall AIMD system that converts 20 kHz acoustic waves into electrical pulse waves to directly stimulate nerves. c) Photographic image of the nerve stimulation system. d) Exploded schematic of the nerve stimulator. e,g) Real photograph of the energy harvesting TENG e), and the pulse generation circuit g). f) Schematic of the CMI–TENG operation mechanism. h) A block diagram of the neurostimulator system.

and generating a reverse pulse (Figure 1f). Figure 1h; and Figure S5, Supporting Information, show how the developed energy creates a pulse wave.[23] The proposed circuit uses a low drop-out circuit to prevent side effects caused by sudden voltage increases of CMI-TENG.

2.2. Fabrication and Characterization of the Triboelectric Layer

We designed a thin composite membrane with high permittivity that could easily vibrate under ultrasound. The membrane was composed of high-permittivity inorganic particles (CCTO) and a high-permittivity polymer matrix (P(VDF–TrFE)). The CCTO, a novel electroceramic material with a high dielectric permittivity of ≈10 200 at room temperature (RT), was embedded in the P(VDF–TrFE) matrix.[24] Composite of high dielectric matrix and particles can improve the device's output by enhancing the charge trapping capability and decreasing the output impedance, enabling real-time driving of the neurostimulation circuit.

Figure 2a shows a schematic of the P(VDF–TrFE):CCTO composite. To confirm that CCTO particles were well embedded in the P(VDF–TrFE) matrix, we conducted a microstructure analysis using field emission scanning electron microscopy (FE-SEM) (Figure 2b). The composite membrane was of 10 μm thickness. The embedded CCTO particles were (1–2) μm in size. To investigate the elemental compositions of the composite membrane, energy dispersive X-ray spectroscopy (EDS) analysis was performed (Figure 2c; and Figure S6, Supporting Information). Ca, Cu, Ti, and O elements were detected at the position of the CCTO particle, while elemental compositions of P(VDF–TrFE), such as C and F, were detected at the matrix position. We also investigated the surface morphology of composite membranes with different concentrations of CCTO (Figure S7, Supporting Information). The surface roughness was increased when we embedded CCTO particles. Because the P(VDF-TrFE):CCTO composite was softly placed on the electrode and the layer has its surface roughness, the air gap still exists for the ultrasound-driven mechanical vibration.[19]

Figure 2d shows the circuit configuration of the neurostimulation system. Where the applied voltage value is fixed by the neurostimulation circuit, the minimum supplied voltage generated by the TENG is determined according to the output impedance of the TENG. Based on the device's structure, when we measure the inductance, capacitance, and resistance with an LCR meter, our device demonstrates exclusively capacitive characteristics. Our device, lacking resistance or inductive components, has an output impedance identical to the capacitive impedance. Therefore, to achieve a lower output impedance, the

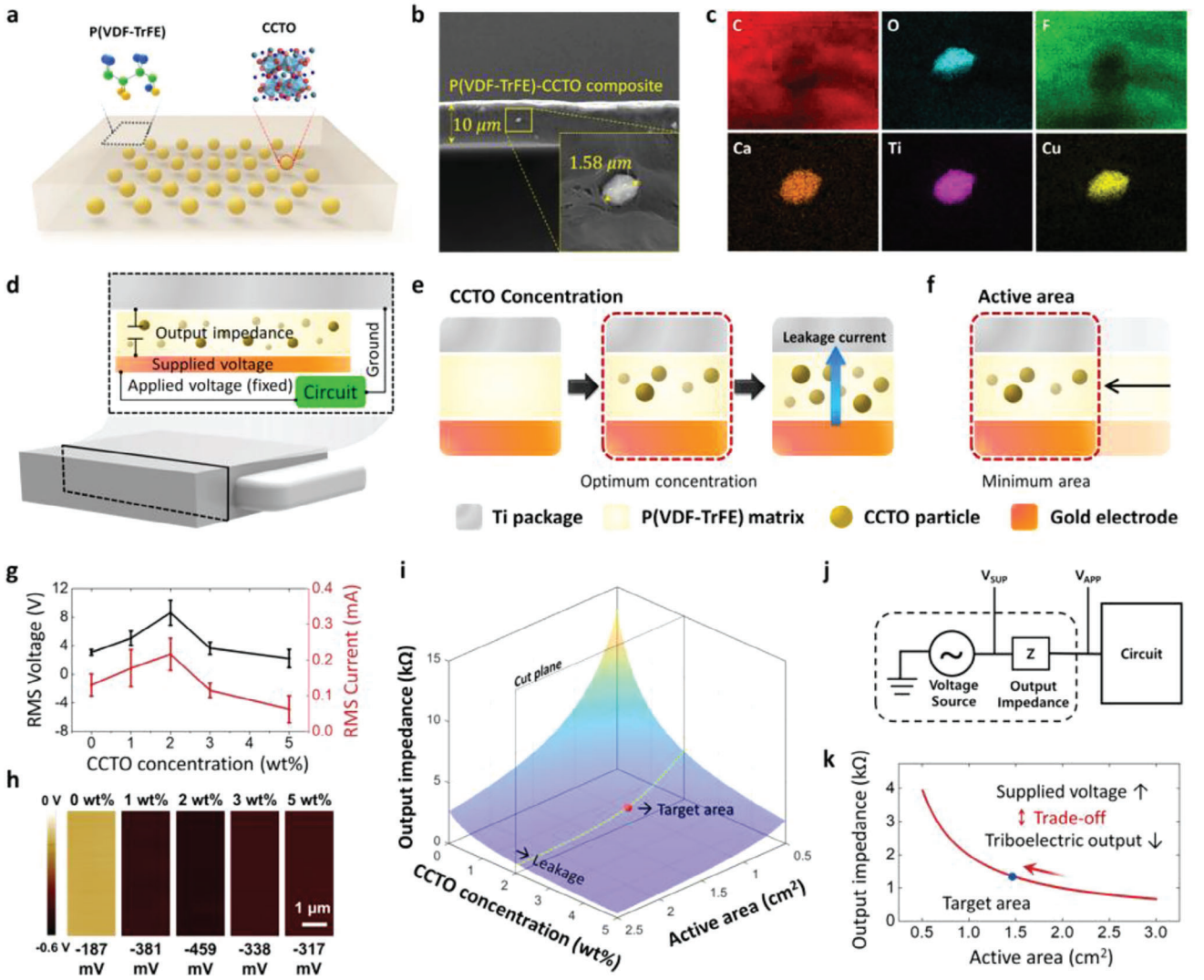

Figure 2. Triboelectric characterization of design. a) Schematic of the P(VDF–TrFE):CCTO composite membrane. b) Cross-sectional view of FE-SEM image of the composite membrane. c) Element mapping profiles of CCTO particle in P(VDF–TrFE) matrix measured by EDS. d) Cross-sectional schematics illustrating the CMI–TENG integrated neurostimulator system. e,f) Methodologies to decrease the output impedance of the TENG (CCTO concentration e) and active area f) control). g) Plotted root mean square voltage and current values of the CMI–TENG as a function of CCTO concentration varying (0–5) wt%. h) KPFM images showing the CPD values of composites and concentration of CCTO. i) 3D Plot of the calculated output impedance as a function of the area of the device and the concentration of CCTO. j) Electrical model of the CMI–TENG-based AIMD. k) Output impedance plot as a function of the active area when the concentration of CCTO is 2 wt%.

capacitance should be increased. Consequently, both the device's area and the CCTO concentration can be adjusted, as shown in Figure 2e,f. However, as the concentration of CCTO increased, the CCTO particles tended to aggregate. Aggregated particles can create a leakage current path.[25] Therefore, enhanced output performance due to increased permittivity can be canceled out by leakage currents, due to an excessive CCTO concentration.[26] To verify the maximum concentration of CCTO, we measured the triboelectric output under ultrasound. The device was placed at 5 mm below an ultrasound probe in water, and irradiated by 20 kHz ultrasound at an intensity of 500 mW cm^{-2}. Figure 2g; and Figure S8, Supporting Information, show the TENG has maximum voltage and current at 2 wt% concentration. We further investigated the effect of CCTO concentration on the triboelectric output performance by measuring the surface potential of the composites using Kelvin probe force microscopy (KPFM) (Figure 2h). As the concentration of CCTO increased to 2 wt%, the surface potential of the P(VDF–TrFE):CCTO composites decreased. However, when the concentration of CCTO was further increased, the surface potential increased. When the surface potential difference between two triboelectric materials becomes larger, a better TENG output performance has been reported.[27] The double electrode triboelectric output by pushing tester also shows a similar tendency (Figure S9, Supporting Information). To confirm that the decrease in output is caused by leakage current, we further examined the triboelectric output

in single electrode mode using a pushing tester (Figure S10, Supporting Information). Unlike the results from the double electrode mode, the triboelectric output increased and saturated as the CCTO concentration increased. Thus, we can conclude that the addition of 2 wt% CCTO in P(VDF−TrFE) matrix is optimum for the triboelectric output of the device.

As the concentration of filler increases, the Young's modulus of the composite membrane can change, which can result in acoustic impedance change. Since ultrasound energy transmission depends on the difference in acoustic impedance of two media (e.g., ultrasound gel and the composite), the Young's modulus should be considered when confirming that the electrical output difference along the concentration of CCTO is not due to an acoustic impedance change. We evaluated the Young's modulus of the composite as a function of the concentration of CCTO using a universal testing machine (UTM) (Figure S11, Supporting Information). When the concentration of CCTO ranged (0–5) wt%, all composite membranes showed similar Young's modulus (≈ 1.04 GPa). Therefore, we could confirm that the electrical output enhancement was not attributable to the difference in Young's modulus between the composite membranes.

In the situation where the optimum concentration of CCTO was determined, the output impedance according to the CCTO concentration and active area was calculated to determine the active area of the device (Figure 2i; and Note S3, Supporting Information). To determine the output impedance of our device, which exhibits solely capacitive characteristics as previously described, we calculated the capacitive impedance. The calculated dielectric constant shows similar tendency with dielectric constant measurement (Figure S12, Supporting Information). The P(VDF−TrFE):CCTO composite has 3 times larger dielectric constant compare to the P(VDF−TrFE) film. When designing an invasive neurostimulator, we needed to design a TENG with the minimum active area where the circuit could be operated. As the active area of the TENG decreases, the required supplied voltage increases, but the triboelectric output decreases (Figure 2j,k). According to this correlation, we determined the active area of the device.

2.3. Operation and Ti Package of the CMI-TENG-Based AIMD

To confirm the real-time operation of AIMD depending on the active area, we checked whether the Ti-packaged CMI−TENG could provide sufficient energy to the electrical circuit designed for neurostimulation in various environments (**Figure 3**a,b; and Figure S13, Supporting Information). Figure 3c,d; and Figures S14 and S15, Supporting Information, show the root mean square (RMS) voltage measured in open-circuit condition (40 Megohm impedance), and the RMS current measured in short-circuit condition of the CMI−TENG, depending on the Ti package (Movies S1 and S2, Supporting Information). The CMI-TENG was able to generate average voltage of 21.99 V and current of 0.697 mA peak-to-peak value under water. These results correspond to RMS voltage of 6.91 V and RMS current of 0.182 mA. These results have the highest energy transmission efficiency compared to other literatures (Figure 3e).[17,18,19,28,29,30] As a result of measuring the output under various environments, the output of the CMI−TENG decreased when we packaged our device with Ti. The decreased output was possibly attributable to the attenuation of ultrasound intensity due to the ultrasound's reflection, scattering, and absorption. Although the output of the TENG in the Ti packaging decreased, the mechanical stability of the neurostimulator was improved. To verify that the Ti package can protect the device from unexpected physical force, we carried out finite element method (FEM) simulations. It was confirmed that the internal stress of the device was concentrated on Ti in a situation where an external force of 100 kPa pressed the neurostimulator (Figures S16 and S17, Supporting Information).

Considering the power reduction effect of Ti, we prepared three TENGs with different areas to determine the active area of the TENG (Figure 3f). Each TENG showed a minimum supplied voltage of (1.23, 1.79, and 2.65) V of (2.0×2.0 cm^2, 1.2×1.2 cm^2, and 0.8×0.8 cm^2) of (0.5, 1.3, and 3.0) kilohms, respectively, which values were inversely proportional to the active area (Figure 3g). Although the TENG with the smallest area did not generate sufficient supplied voltage, it satisfies the conditions for driving the circuit, as it exceeds the active area of 1.2×1.2 cm^2 (Figure 3h,i). Therefore, we determined the minimum active area for driving the neurostimulation circuit. For practical application in vivo, operational stabilities of the AIMD were investigated. Since we designed a nerve stimulation protocol with 5 min stimulation periods, continuous operation of the AIMD was observed for 5 min. The device showed excellent durability, generating stable pulses in the range (1.4–1.6) V at a frequency of 2 Hz (Figure 3j; and Movie S3, Supporting Information).

2.4. In Vitro and In Vivo Biocompatibility Evaluation of the Neurostimulator

To verify biocompatibility, we cultured human fibroblast cells (CRL-1502) on the Ti-packaged neurostimulator in a typical culture dish for 72 h. Immunofluorescent staining results showed that CRL-1502 proliferated well on the Ti, and that the cells in both media had similar density and morphology (**Figure 4**a; and Figure S18, Supporting Information). No dead or distorted cells could be observed on the Ti. We then checked the viability of CRL−1502 cells through 3-{4,5-dimethylthiazol-2-thiazolyl}−2,5-diphenyl-2, H-tetrazolium bromide (MTT) assay (Figure 4b). Compared to the control group, the normalized viability of CRL−1502 cells on Ti was 1.2 times higher after 72 h. In the same way, cell viability of the P(VDF−TrFE):CCTO triboelectric layer was also checked. As shown in Figure S19, Supporting Information, there was no significant difference in cell viability between the control group and the triboelectric layer. A Comet Assay was performed to determine whether Ti was genotoxic, causing DNA damage (Figure 4c). Compared to the control group, Ti did not induce DNA damage, as indicated by no difference in DNA tail length for CRL−1502 (skin fibroblast) cells (Figure 4d). After confirming the biocompatibility of Ti, we inserted the neurostimulator into rats (Figure 4e). Considering the distance to the stimulating nerve, the bladder pressure recording system, and the area of the ultrasound probe, we determined the implant location of the nerve stimulator (Figure 4f,g). To check the inflammatory response of the device after implantation, we stained hematoxylin-eosin (H&E) on the subdermal tissue in the implanted part at 3 days (Figure 4h; and Figure S20, Supporting

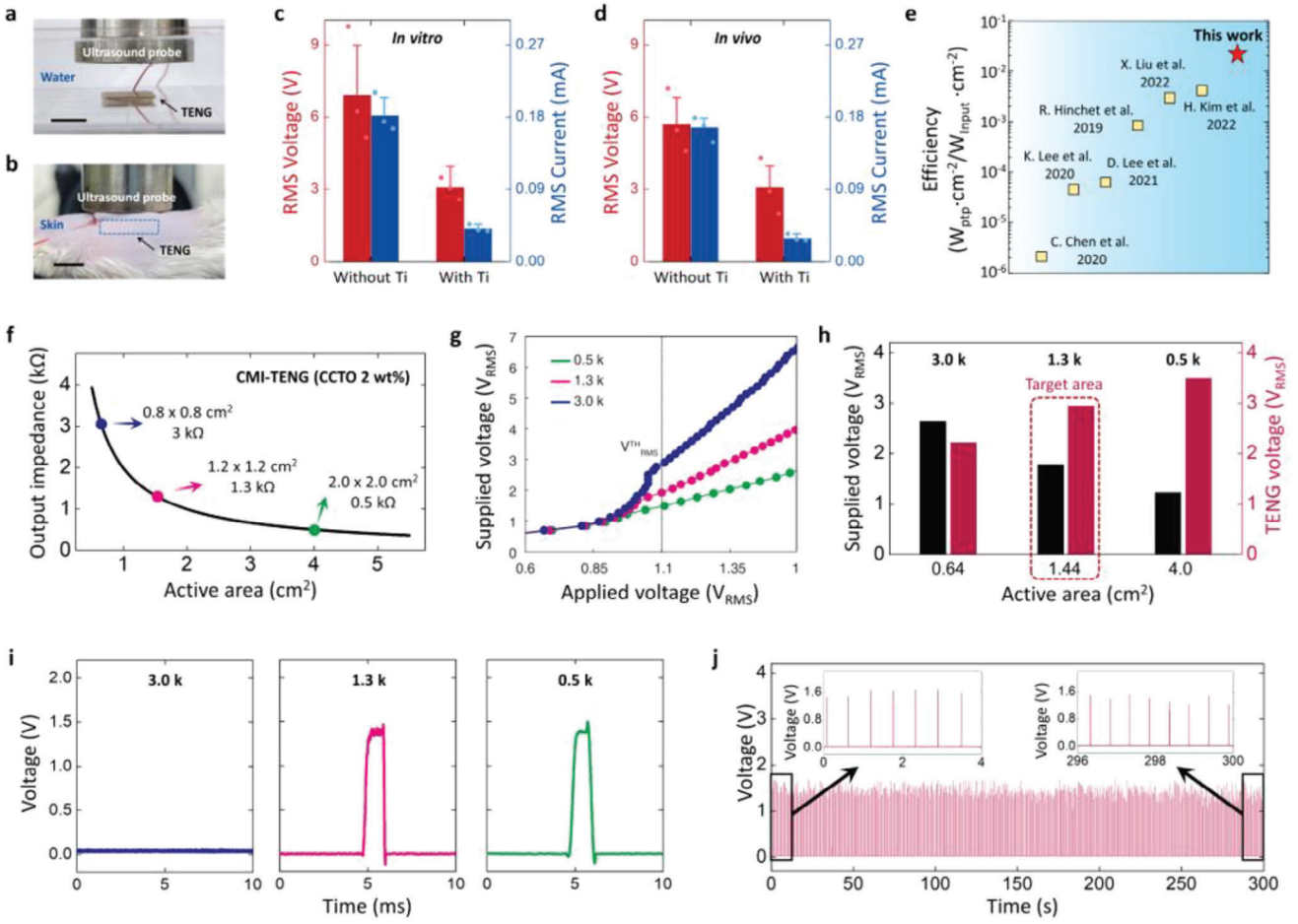

Figure 3. Characterization of the Ti-packaged CMI–TENG for application to AIMD. a,b) Experimental setup picture for output characterization of CMI-TENG under 20 kHz ultrasound in water a) and under the skin of a rat b) (scale bar = 1 cm). c,d) RMS Voltage outputs (red) in open-circuit condition and RMS current outputs (blue) in short-circuit condition measured in water at 5 mm from the ultrasound probe c) and under the skin of a rat d) (bars: mean ± sd). Outputs are divided into those without (left) and with (right) Ti package. e) Energy transfer efficiencies of ultrasound energy harvesting using TENGs. f) Output impedance decreased by the active area of the CMI-TENG. g) The required supplied voltage for applying voltage to the circuit increases by the output impedance of the device. 1.1 RMS voltage (V^{TH}_{RMS}, gray line) is required to be applied to the circuit for operation. h) The required supplied voltage and TENG voltage output by the active area of the CMI-TENG. i) Pulse wave signal from the stimulator circuit powered by TENGs with different output impedance. j) Steady pulse wave signals from the TENG-AIMD monitored for 5 min.

Information). Some inflammatory reactions were seen around the device implanted site. However, similar biological reactions occurred with a commercialized product. Also, to confirm potential damage caused by ultrasound, we irradiated rat skin with an ultrasound intensity of 500 mW cm^{-2}. H&E test results showed no significant changes in the skin, even after 1 h of exposure. (Figure S21, Supporting Information). Rats showed normal daily behavior, without severe fever or suppuration (Movie S4, Supporting Information), consistent with a previous study.[31]

2.5. Preclinical Evaluation for Controlling Bladder Function

We performed a preclinical study with our developed system for treating overactive bladder by stimulating the tibial nerve near the lower ankle of rats. The lower ankle is a well-known stimulation target to treat an overactive bladder.[1] Physiological modulation of bladder function using the proposed system was monitored through cystometry with a free-moving awake rat (Movies S5, S6 and Figure S22, Supporting Information). The cystometry continuously presented bladder pressure and voiding volume when saline solution was infused at a constant rate into the bladder through an intravesicular catheter (Movies S7, S8 and Figure S23, Supporting Information). Bladder function recordings indicated that the tibial nerve stimulation applied by our device suppressed the bladder activity, and thus increased the urination period and the bladder capacity (**Figure 5**a). Representative graphs in Figure 5b show the stimulation-induced effects on bladder function. The urination period and bladder capacity were evaluated with the inter-urination interval and the voiding volume per urination, respectively. After the stimulation, both the inter-urination interval and the voiding volume per urination were significantly increased (Figure 5c,d). The inter-urination interval increased from (131.8 ± 15.2) s in prestimulation baseline

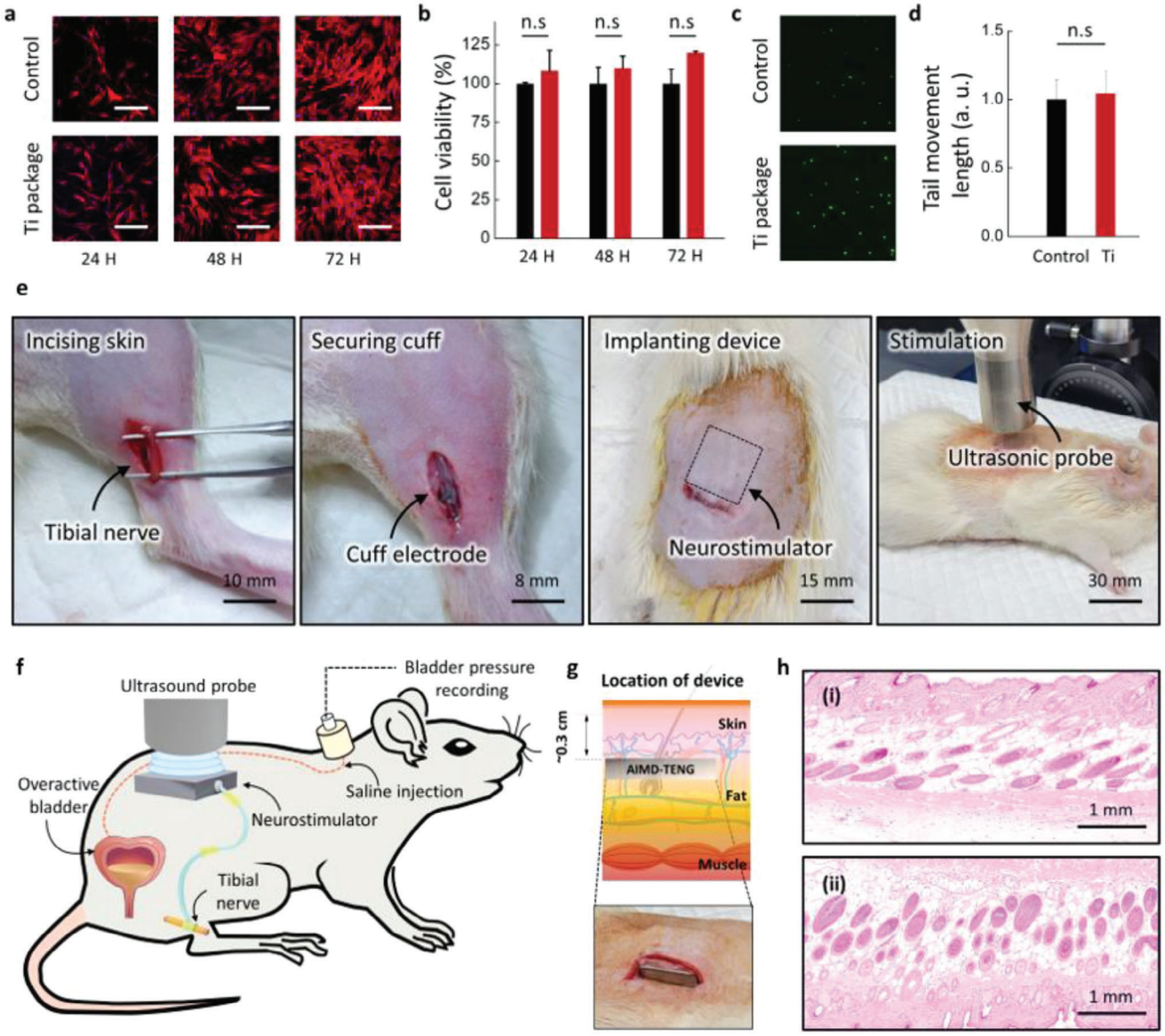

Figure 4. Biocompatibility of the nerve stimulation system. a) Immunofluorescence image of stained human fibroblast cells (CRL-1502) cultured on a typical culture dish and Ti for 72 h (scale bar = 200 μm). b) Normalized cell viability for 72 h of typical culture dish and Ti (bars: mean ± sd). c) In vitro DNA damage evaluated using Comet Assay. d) Normalized genotoxicity of human fibroblast cells (CRL-1502) and Ti. e) *vivo* experiment procedure of the nerve stimulation system. f) Schematic illustrating in vivo experiment of the nerve stimulation system implanted in a rat. g) Schematic of the tissue showing the location of the nerve stimulator. h) H&E staining of subdermal tissues in the implanted part.

to (277.6 ± 134.1) s after stimulation ($p < 0.001$). The voiding volume increased from (0.23 ± 0.05) g at prestimulation baseline to (0.34 ± 0.12) g after stimulation ($p < 0.05$). These results agree with clinical evidence for treating the overactive bladder with tibial nerve stimulation, which is well-known to increase urination period and bladder capacity.[32,33] This clinical effectiveness was validated through comparative analysis with bladder function changes in control groups that underwent sham stimulation. The control group consisted of a group that has not implanted any devices and a group that has implanted dummy devices lacking the internal neurostimulator circuit. As shown in Figure S24 (Supporting Information), both groups exhibited no changes in the inter-urination interval after the sham stimulation ($p = 0.19$ for no device group and $p = 0.49$ for dummy device group). The voiding volume decreased after the sham stimulation for no device group ($p < 0.01$), which was even associated with a counter reaction of bladder inhibition, and did not change for dummy device group ($p = 0.89$). These findings clearly indicate that the sham stimulation did not inhibit bladder functions from the same protocol as our developed device. Moreover, the contraction pressure and the threshold pressure showed no substantial changes after stimulation, compared to those pre-stimulation (Figure 5e,g). The contraction pressure changed from ((74.7 ± 2.2) to (75.0 ± 7.5)) mmHg ($p = 0.44$). The threshold pressure changed

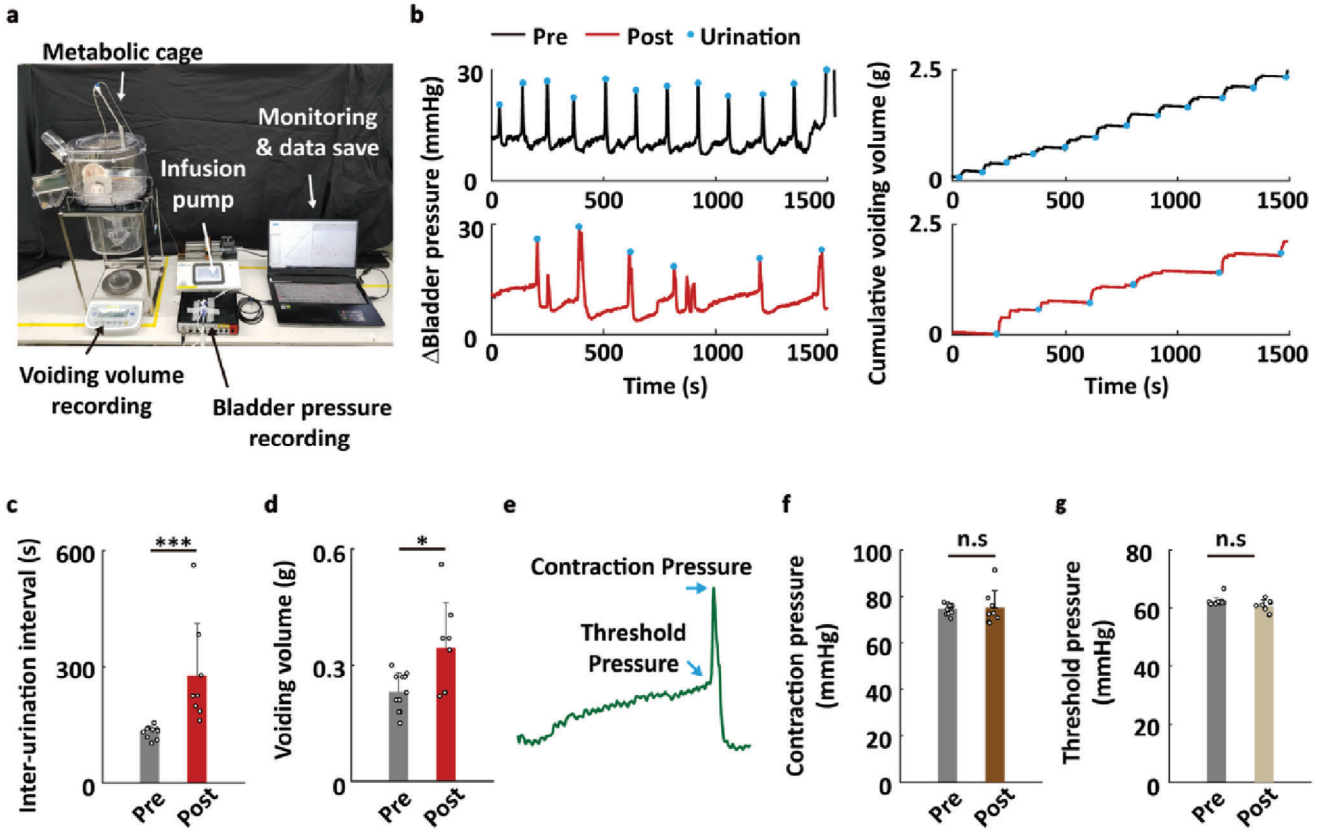

Figure 5. Modulation of bladder activity by the wireless TENG-powered battery-free nerve stimulator. a) Experimental setup picture for awake free-moving cystometry to continuously monitor the bladder function before and after tibial nerve stimulation using the implanted TENG-powered nerve stimulator. Cystometry measured the rat's bladder pressure and voiding volume. b) Traces of bladder pressure and cumulative voiding volume collected before (black), and after (red), stimulation (blue circles: occurrence of urination). c) Inter-urination interval before and after stimulation (bars: mean ± sd; gray bar: pre; red bar: post; white circles: raw data points). d) Voiding volume before and after stimulation. e–g, Non (or slightly) modulated bladder functions after stimulation (contraction pressure, and threshold pressure): e) Conceptual illustration of each bladder function. f) Contraction pressure. g) Threshold pressure. The number of samples was 11 for prestimulation, and 8 for poststimulation. $*p < 0.05$, $**p < 0.01$, $***p < 0.001$, Mann–Whitney U-test.

from ((62.2 ± 1.4) to (60.6 ± 2.1)) mmHg ($p = 0.10$). These results indicated that the developed wireless TENG-powered battery-free neurostimulator did not induce urodynamic side effects, such as decrease in compliance or contraction amplitude.[34] This evidence strongly supports both the effectiveness and safety of our neuro stimulator for treating an overactive bladder disorder.

3. Conclusion

Herein, we report the materials, designs, and systems for battery-free, wireless-powered, and hermetically-encapsulated implantable neurostimulators with the ultrasound-driven energy harvester CMI–TENG suggested in this study. In contrast to previously reported ultrasound-driven TENGs that should store generated energy into bulky batteries,[18] we developed a battery-free system based on the beneficial characteristics of CMI–TENG, which showed high capacitance. The triboelectric layer composed of high-k materials both improved charge trapping capability, and remarkably lowered the impedance of the CMI–TENG itself. These factors make it possible to efficiently transfer energy into the low-impedance stimulator circuit, without the energy-storing battery. Its energy transmission efficiency is the highest among those reported so far. When operating the CMI–TENG, we used ultrasound at a power intensity of 500 mW cm^{-2}, which would be suitable for human use (Note S2, Supporting Information), and this low power requirement provides the potential feasibility that the transducer for our developed system could be enough compact and lightweight to be portable. Moreover, our system uses Ti as the packaging material that is still the only proven encapsulation solution for clinically-approved implantable medical devices due to its outstanding hermeticity to protect electrical circuits inside body. The stimulator circuit was successfully operated with the Ti package, unlike other wireless energy technologies with low energy transmission efficiency. Preclinical assessment for the battery-free and Ti-packaged neurostimulator powered by CMI–TENG was performed through in vivo experiments that measured the stimulation-induced bladder function modulation. The device was implanted on a rat model, and the bladder functions of the rat were monitored in free-moving condition before and after stimulation. Our results agreed with previously reported experimental evidence meaning the effective treatment

of bladder dysfunctions, and thus showed the effectiveness of the proposed device in restoring bladder functions from urinary disorders, such as OAB.[29,30] The technical advances reported herein strongly suggest that the proposed battery-free device system based on CMI–TENG is a promising solution toward the permanent implantation of bioelectric devices to treat various chronic dysfunctions, while translational study to verify their long-term safety and stability still needs to be performed.

4. Experimental Section

Materials Preparation: Figure S3, Supporting Information, describes the membrane fabrication process. The P(VDF–TrFE) solution was prepared by dissolving the P(VDF–TrFE) copolymer with a 70/30 (%/%) molar ratio (Piezotech Arkema, France) in *N,N*-dimethylformamide (DMF, Sigma-Aldrich). After a solution of P(VDF–TrFE) matrix (≈10 wt%) was prepared, a certain fraction of CCTO particles was blended using stirring. Then, an ultrasonication process was carried out for 30 min in an ultrasonication bath. Once the CCTO particle dispersed P(VDF–TrFE) was prepared, it was coated on a glass substrate using an automatic bar coater. To eliminate residual pores in the coated solution, vacuum degassing in a vacuum oven was conducted. The coated solution was then dried at 60 °C on a hot plate to remove the DMF solvent, followed by annealing at 140 °C for 2 h. After naturally cooling to RT, the P(VDF–TrFE):CCTO composite membrane was peeled off of the glass substrate.

Materials Characterization: To study the microstructure of the composite, FE-SEM (JSM–IT800) and EDS measurements were performed. Topography and KPFM measurements were conducted using Park Systems XE-100 with Multi75E-G tip (BudgetSensors). A 2 V AC voltage at 17 kHz was applied to the AFM tip, and a 5 × 5 μm^2 size area was scanned at a rate of 0.3 Hz.

Device Fabrication: Figure S2, Supporting Information, describes the device fabrication process. The device consisted of a P(VDF–TrFE):CCTO composite membrane and a PCB substrate whose FR-4 glass epoxy layer was covered by Cu and Au. To solder wire on the back side of the PCB, a hole plugging land (HPL) PCB was used, whose top and bottom layers were electrically connected via a hole. The composite membrane was placed on the device and attached using ethylene-vinyl acetate based hot melt adhesive.

Electrical Characterization: Voltage signals were measured using a digital phosphor oscilloscope (Tektronix, DPO 3052 Digital Phosphor) with a voltage probe (Tektronix P5100A) of 40 MΩ input impedance. Current signals were measured using a low noise current amplifier (FEMTO, DLPCA-200). To explore the triboelectric characteristics of the composite, a pushing tester (Z-Tech, ZPS-100) was used for regular application of mechanical force. Ultrasound generation and characterization were carried out using a commercial ultrasonic transducer and generator (Mirae MV100).

TENG Energy Harvesting and Neurostimulating Circuit: We made an 8 × 8 mm^2 size battery-free (passively operating) electronic circuit by harvesting TENG energy (Figure 1g).[23] After energy-harvesting, the circuit generated monophasic square pulse trains for neurostimulation. Components of the circuit included the following (Figure 1h): 1) a half-wave voltage doubler to rectify the input signal generated by the TENG module, 2) a voltage regulator (Low-dropout, LDO) to supply stable voltage to the pulse-generator module in the next step, 3) an asymmetrical square pulse generator (stable multivibrator with different charging/discharging time constants), and 4) another voltage regulator after the pulse generator to stably load output stimulation.

System Integration and Device Manufacturing: The implantable nerve stimulator device wirelessly powered by TENG and packaged by Ti case was manufactured by integrating hardware systems consisting of the fabricated TENG module, the electronic circuit module, Ti encapsulation cases, a bi-polar feedthrough, and a cuff nerve electrode (Figure S4, Supporting Information). The TENG module could transform ultrasound energy into electrical energy. The circuit module could harvest electrical energy from the TENG module, and generate nerve-stimulating unipolar pulses with a frequency of 2 Hz and a pulse width of 1 ms. The Ti cases were fabricated with grade 2 Ti, and customized as a bottom box having one side open and a top cover plate (machined and provided by Osong Medical Innovation Foundation, Rep. of Korea). The feedthrough (SA-270921, Morgan Advanced Materials) consisted of an inner layer of ceramic, and an outer layer of Ti. The outer layer was laser-welded onto the Ti case. Cuff electrode wires were platinum/iridium bipolar, and encapsulated with biocompatible silicone (electrode was customized and provided by Microprobes for Life Science Inc.). The TENG module was first attached on the inner side of the top Ti plate using PDMS as an adhesive to avoid air layer intercepting between the TENG and the plate. The circuit board was placed and fixed inside the box case. Its anode and cathode pins were connected to feedthrough wires interconnecting the inside and the outside of the Ti case, while protecting from in vivo fluid and moisture penetrating inside the case.[35] A Cu wire connected to the Au/Ni electrode layer of TENG module was soldered at the input pin of the circuit board. Outer feedthrough wires were connected to the electrode. Metal exposure at the connecting part was then encapsulated with biocompatible silicone adhesive (Kwik-Sil, World Precision Instruments).

Experimental Subjects: Animal experiments were performed using healthy adult male Sprague–Dawley rats (weight: (250–450) g; age: 8–11 weeks; bred and distributed by Orient Bio, Rep. of Korea). This study was reviewed and approved by the Institutional Animal Care and Use Committee (IACUC) of Pohang University of Science and Technology (POSTECH-2021-0099), which is an Association for Assessment and Accreditation of Laboratory Animal Care International (AAALAC International)-accredited facility and abides by the Institute of Laboratory Animal Resources (ILAR) guide. It was performed following guidelines established by the National Institutes of Health. At the end of experiments, rats were euthanized using CO_2 gas.

Surgical Procedure: Surgeries were divided into two steps: 1) bladder catheterization for bladder function monitoring, and 2) device implant. All surgeries were performed under anesthesia induced with isoflurane 5% and O_2 0.3–0.5 L min^{-1} for (5–10) min, and sustained with isoflurane (1–2)%. The bladder was catheterized using a PE 50 tube (BTPE-50, Instech), after incising the lower abdominal region of rat, exposing the bladder, and puncturing a hole on the bladder dome (Figure S22a, Supporting Information).[28] Before exposure of the bladder, the abdominal region was shaved, to prevent any infection by hair entering the surgical site. The skin was also sterilized. The catheterized tube was secured with a purse string suture.[36] The absence of leakage was then confirmed by infusing saline solution (< 1 mL) to inflate the bladder (Figure S22b, Supporting Information). The tube subcutaneously passed to near the neck. It was put on an access button (VABR1B/22, Instech) separately interconnecting to a fluid swivel system. The body of the integrated device was implanted under the skin of the back, and the electrode was placed near the lower ankle with its cuff implanted on the tibial nerve (Figure S22c, Supporting Information). The bladder, muscle, and skin were sutured with braided silk (SK610, Ailee Co., Rep. of Korea). All subjects took recovery period of at least 1 day after surgeries. It was determined that subjects almost recovered their original conditions (Figure S22d, Supporting Information).

Awake Free-Moving Cystometry: A customized free-moving cystometry platform (Figure 5a; and Figure S23a, Supporting Information) consisted of a metabolic cage (C-72R-K, Jung-do B&P, Rep. of Korea), a swivel system (swivel kit: KVABR1T/22 and swivel arm: CM375KRP, Instech), a pressure transducer with its data acquisition device (transducer: BP-102 and DAQ: IX-RA-834, iWorx), a digital weight scale (HS5002, Hansung Instrument, Rep. of Korea), a constant infusing syringe pump (Legato 210P, KD Scientific), and a PC, where recorded data were saved. The swivel system, pressure transducer, and infusing pump were connected using a 3-way Y connector (SCY22, Instech). For cystometry, subjects were first anesthetized with isoflurane (1–2) % O_2 at (0.3–4) L min^{-1} for about 30 min. Anesthesia was stopped, and subjects were moved to a metabolic cage. The access button on the neck of subjects was connected to the swivel system, and saline solution was continuously infused into the bladder (100 ϵL min^{-1}) with an infusing pump. Change of bladder pressure by expansion and contraction of the bladder due to micturition

reflex was continuously recorded with the pressure transducer at a sampling rate of 1 Hz. Pressure data acquired with the transducer DAQ were monitored with its own software (LabScribe, iWorx) on the PC. A weight scale measured the cumulative voiding volume by recording the weights of urine drops. Weight data were transferred to the PC through an RS-232 cable, and presented by open software (RsWeight, A&D Company). Both recordings were simultaneously performed over (1–2) h.

Tibial Nerve Stimulation: An ultrasound transducer (MV100, Mirae, Rep. of Korea)[18] was placed on the skin with an ultrasound gel (Ecosonic, Sanipia) right over the implanted device. The device was operated by <power mW cm^{-2}> ultrasound input. Stimulation was applied for 30 with 5 min of resting period between 5 min stimulation periods. After the stimulation was over, subjects were moved back to the metabolic cage, and their bladder functions were monitored by cystometry for (1–2) h (Figures S20b and S20c, Supporting Information).

Bladder Function Analysis: Bladder pressure and cumulative voiding volume data were each extracted in ".mat" and ".csv" formats, respectively. All data were then analyzed using Matlab (MathWorks). Micturition reflex (urination) points were identified as peaks in the bladder pressure and step increases in cumulative voiding volume. Irregular points not having synchronization between pressure peak and volume increase were excluded, as they could be considered as a non-urination contraction of bladder, or a passive leakage of urine. Urination points for the first 15 min were not counted, to avoid isoflurane effects that might remain after the anesthesia was over. Time intervals between two consecutive urinations (defined as the "inter-urination interval") and voiding volumes for each urination were used to quantitatively compare bladder functions before and after tibial nerve stimulation. In addition, threshold pressure and contraction pressure were calculated for each urination (Figure 5). The threshold pressure was defined as the pressure right before urination peak. The contraction pressure was defined as the maximum peak pressure during urination.

Statistical Analysis: As for bladder functions, the urination interval and the voiding volume of each urination before and after stimulation were compared. Non-normality of data was verified using one-sample Kolmogorov–Smirnov test at the 5% significance level. Thus, comparison of the bladder function between pre- and poststimulation was performed using Mann–Whitney U-test. Significance levels were defined at $p < 0.05$, $p < 0.001$, and $p < 0.005$. They are marked as one, two, and three asterisks for visual simplicity. $p > 0.05$ was considered as statistically nonsignificant, and marked as "n.s."

Supporting Information

Supporting Information is available from the Wiley Online Library or from the author.

Acknowledgements

Y.-J.K., J.L., J.-H.H. contributed equally to this work. This research was supported by the Basic Science Research Program (No. 2022R1A3B1078291), the Pioneer Research Center Program (No. 2022M3C1A3081294) and the Bio & Medical Technology Development Program (No. 2022M3E5E9082206) through the National Research Foundation of Korea (NRF) funded by the Korean government (MSIT). S.-W.K. acknowledged the Yonsei Fellow Program funded by Youn Jae Lee.

Conflict of Interest

The authors declare no conflict of interest.

Data Availability Statement

The data that support the findings of this study are available from the corresponding author upon reasonable request.

Keywords

implantable devices, neurostimulation, overactive bladder, triboelectric implants, ultrasound energy harvesting

Received: July 20, 2023
Revised: October 9, 2023
Published online:

[1] P. Limousin, T. Foltynie, *Nat. Rev. Neurol.* **2019**, *15*, 234.
[2] D. M. Andrade, D. Zumsteg, C. Hamani, M. Hodaie, S. Sarkissian, A. M. Lozano, R. A. Wennberg, *Neurology* **2006**, *66*, 1571.
[3] T. Cameron, *J. Neurosurg. Spine* **2004**, *100*, 254.
[4] L. L. de Wall, J. P. Heesakkers, *Res. Rep. Urol.* **2017**, *9*, 145.
[5] K. Agarwal, R. Jegadeesan, Y.-X. Guo, N. V. Thakor, *IEEE Rev. Biomed. Eng.* **2017**, *10*, 136.
[6] H.-J. Yoon, S.-W. Kim, *Joule* **2020**, *4*, 1398.
[7] L. Lu, Z. Yang, K. Meacham, C. Cvetkovic, E. A. Corbin, A. Vázquez-Guardado, M. Xue, L. Yin, J. Boroumand, G. Pakeltis, *Adv. Energy Mater.* **2018**, *8*, 1703035.
[8] S. Han, F. Jiao, Z. U. Khan, J. Edberg, S. Fabiano, X. Crispin, *Adv. Funct. Mater.* **2017**, *27*, 1703549.
[9] S. M. Won, L. Cai, P. Gutruf, J. A. Rogers, *Nat. Biomed. Eng.* **2023**, *7*, 405.
[10] Y. S. Choi, R. T. Yin, A. Pfenniger, J. Koo, R. Avila, K. B. Lee, S. W. Chen, G. Lee, G. Li, Y. Qiao, A. Murillo-Berlioz, A. Kiss, S. Han, S. M. Lee, C. Li, Z. Xie, Y.-Y. Chen, A. Burrell, B. Geist, H. Jeong, J. Kim, H.-J. Yoon, A. Banks, S.-K. Kang, Z. J. Zhang, C. R. Haney, A. V. Sahakian, D. Johnson, T. Efimova, Y. Huang, et al., *Prilozi - Maked. Akad. Nauk. Umet., Odd. Prir.-Mat. Bioteh. Nauki* **2021**, *39*, 1228.
[11] C. Y. Kim, M. J. Ku, R. Qazi, H. J. Nam, J. W. Park, K. S. Nam, S. Oh, I. Kang, J.-H. Jang, W. Y. Kim, J.-W. Jeong, *Nat. Commun.* **2021**, *12*, 535.
[12] P. Gutruf, V. Krishnamurthi, A. Vázquez-Guardado, Z. Xie, A. Banks, C.-J. Su, Y. Xu, C. R. Haney, E. A. Waters, I. Kandela, S. R. Krishnan, T. Ray, J. P. Leshock, Y. Huang, D. Chanda, J. A. Rogers, *Nat. Electron.* **2018**, *1*, 652.
[13] J. A. Guggenheim, J. Li, T. J. Allen, R. J. Colchester, S. Noimark, O. Ogunlade, I. P. Parkin, I. Papakonstantinou, A. E. Desjardins, E. Z. Zhang, P. C. Beard, *Nat. Photonics* **2017**, *11*, 714.
[14] C. Demené, J. Robin, A. Dizeux, B. Heiles, M. Pernot, M. Tanter, F. Perren, *Nat. Biomed. Eng.* **2021**, *5*, 219.
[15] V. Cotero, J. Graf, H. Miwa, Z. Hirschstein, K. Qanud, T. S. Huerta, N. Tai, Y. Ding, K. Jimenez-Cowell, J. N. Tomaio, W. Song, A. Devarajan, T. Tsaava, R. Madhavan, K. Wallace, E. Loghin, C. Morton, Y. Fan, T.-J. Kao, K. Akhtar, M. Damaraju, L. Barenboim, T. Maietta, J. Ashe, K. J. Tracey, T. R. Coleman, D. D. Carlo, D. Shin, S. Zanos, S. S. Chavan, et al., *Nat. Biomed. Eng.* **2022**, *6*, 683.
[16] L. Jiang, G. Lu, Y. Yang, Y. Zeng, Y. Sun, R. Li, M. S. Humayun, Y. Chen, Q. Zhou, *Energy Environ. Sci.* **2021**, *14*, 1490.
[17] H. S. Kim, S. Hur, D.-G. Lee, J. Shin, H. Qiao, S. Mun, H. Lee, W. Moon, Y. Kim, J. M. Baik, C.-Y. Kang, J. H. Jung, H.-C. Song, *Energy Environ. Sci.* **2022**, *15*, 1243.
[18] R. Hinchet, H.-J. Yoon, H. Ryu, M.-K. Kim, E.-K. Choi, D.-S. Kim, S.-W. Kim, *Science* **2019**, *365*, 491.
[19] D.-M. Lee, N. Rubab, I. Hyun, W. Kang, Y.-J. Kim, M. Kang, B. O. Choi, S.-W. Kim, *Sci. Adv.* **2022**, *8*, eabl8423.
[20] S. Niu, Z. L. Wang, *Nano Energy* **2015**, *14*, 161.
[21] S. Niu, X. Wang, F. Yi, Y. S. Zhou, Z. L. Wang, *Nat. Commun.* **2015**, *6*, 8975.
[22] M. Lu, W. Yin, A. Peyton, Z. Qu, X. Meng, Y. Xie, P. Zhao, J. Luo, Q. Zhao, Y. Tao, T. Zhou, Z. Zhang, *Nano Energy* **2019**, *63*, 103883.

[23] K. Kim, S. G. Jang, H. G. Lim, H. H. Kim, S.-M. Park, *IEEE Access* **2021**, *9*, 153850.
[24] M. A. Subramanian, D. Li, N. Duan, B. A. Reisner, A. W. Sleight, *J. Solid State Chem.* **2000**, *151*, 323.
[25] P. Thomas, S. Satapathy, K. Dwarakanath, K. B. R. Varma, *eXPRESS Polym. Lett.* **2010**, *4*, 632.
[26] J. Kim, H. Ryu, J. H. Lee, U. Khan, S. S. Kwak, H. J. Yoon, S.-W. Kim, *Adv. Energy Mater.* **2020**, *10*, 1903524.
[27] S. Cheon, H. Kang, H. Kim, Y. Son, J. Y. Lee, H.-J. Shin, S.-W. Kim, J. H. Cho, *Adv. Funct. Mater.* **2018**, *28*, 1703778.
[28] C. Chen, Z. Wen, J. Shi, X. Jian, P. Li, J. T. W. Yeow, X. Sun, *Nat. Commun.* **2020**, *11*, 4143.
[29] K. H. Lee, Y.-Z. Zhang, Q. Jiang, H. Kim, A. A. Alkenawi, H. N. Alshareef, *ACS Nano* **2020**, *14*, 3199.
[30] X. Liu, Y. Wang, G. Wang, Y. Ma, Z. Zheng, K. Fan, J. Liu, B. Zhou, G. Wang, Z. You, Y. Fang, X. Wang, S. Niu, *Matter* **2022**, *5*, 4315.
[31] H. Ryu, H.-m. Park, M.-K. Kim, B. Kim, H. S. Myoung, T. Y. Kim, H.-J. Yoon, S. S. Kwak, J. Kim, T. H. Hwang, E.-K. Choi, S.-W. Kim, *Nat. Commun.* **2021**, *12*, 4374.
[32] J. Lee, E. Park, W. Kang, Y. Kim, K.-S. Lee, S.-M. Park, *IEEE Trans. Biomed. Eng.* **2020**, *68*, 214.
[33] E. Park, J.-W. Lee, T. Kim, M. Kang, B. H. Cho, J. Lee, S.-M. Park, K.-S. Lee, *Sci. Rep.* **2020**, *10*, 19897.
[34] A. F. Colhoun, J. E. Speich, L. F. Cooley, E. D. Bell, R. W. Barbee, G. Guruli, P. H. Ratz, A. P. Klausner, *World J. Urol.* **2017**, *35*, 1255.
[35] H. Lee, J. S. Mun, W. R. Jung, S. Lee, J. Kang, W. Kang, S. Kim, S.-M. Park, D. L. Na, Y.-M. Shon, S. J. Kim, *IEEE Trans. Biomed. Circuits Syst.* **2020**, *14*, 1393.
[36] P. Uvin, W. Everaerts, S. Pinto, Y. A. Alpízar, M. Boudes, T. Gevaert, T. Voets, B. Nilius, K. Talavera, D. D. Ridder, *J. Vis. Exp.* **2012**, *66*, e3869.